THZ MICROPROBE SYSTEM FOR CONTACT-FREE HIGH-RESOLUTION SHEET RESISTANCE IMAGING

M. Nagel[2,*], A. Safiei[1], S. Sawallich[2], C. Matheisen[2], T. M. Pletzer[1], A.A. Mewe[3], N. van der Borg[3], I. Cesar[3], and H. Kurz[2]
[1]RWTH Aachen University, Institute of Semiconductor Electronics, Sommerfeldstraße 24, D-52074 Aachen, Germany
[2]AMO GmbH, Otto-Blumenthal-Straße 25, D-52074 Aachen, Germany
[3]ECN Solar Energy, Westerduinweg 3, NL-1755 LE Petten, The Netherlands
[*]Corresponding author: nagel@amo.de, phone: +49 241 8867 141, fax: +49 241 8867 560

ABSTRACT: Recently, the demand for non-destructive contact-free measurement tools which are able to measure conductivity distributions independent of surface morphology at spatial resolutions down to a few micrometres has strongly increased. This demand is caused by an increased application of micron-scale doping areas in solar cells (e.g. selective emitter structures or interdigitated back-contact (IBC) cells) and further semiconductor applications. In this work a recently introduced method based on the photoconductive (PC) near-field detection of terahertz (THz) light transmission is introduced for sheet resistance imaging on rough laser-doped multi-crystalline (mc) silicon samples featuring doping microstructures. Furthermore spatially resolved sheet resistance measurements on the backside of IBC solar cells and test structures will be presented. THz and comparative 4-point-probe (4pp) measurements will be presented giving evidence that the terahertz microprobe-based approach can effectively fill the yet present gap of high-resolution contact-free conductivity measurement tools applicable to wafer-scale samples with rough or laser-processed surfaces.

Keywords: selective emitter, laser-doping, interdigitated back-contact, terahertz, characterization, sheet resistance, high-resolution.

1 INTRODUCTION

This work focuses on the introduction of optoelectronic THz-microprobe measurements as a novel approach for quantitative spatially resolved and contactless sheet resistance measurements. Sheet resistance quantification of homogeneous diffusions is a standard practice in solar cell process control, but to date no method is available for diffusion patterns with feature sizes in the range of 10 to 1000 micron independent of surface morphology. This feature size range is gaining relevance for process control of selective emitters and interdigitated back-contact solar cells. Both examples exhibit surfaces with changing surface roughness in the area of interest due to texture and the laser processing [1] and/or etching steps that are intrinsic to the definition of the diffusion patterns. Investigations on large scale laser-doped mc-Si samples and the comparisons to 4pp data are presented. Finally, to demonstrate the resolution potential of the THz microprobe system spatially resolved sheet resistance measurements on laser-doped mc-Si samples and on IBC cells and test structures have been done.

2 EXPERIMENTAL

On top of Fig. 1 the central part of the measurement configuration around the sample used in this work is shown. The measurement system is based on a femtosecond pulsed Ti-Sapphire laser with a wavelength λ of 810 nm, τ = 120 fs pulse duration and a pulse repetition rate of 78 MHz. This laser is used to optically excite the photoconductive (PC) THz emitter and the near-field THz probe in a classic pump/probe scheme described earlier [2]. Time-domain sampling of the transmitted THz signal is accomplished through an opto-mechanical delay-stage. The microstructure of the THz microprobe (depicted at the bottom of Fig. 1) consists of a tapered pair of electrodes patterned on a low-temperature-grown (LT)-GaAs cantilever of 1.3 µm thickness. A constriction of the lateral electrode spacing localised in approx. 100-µm-distance from the tip apex is applied as the PC-switch for THz field sampling. The tip is held in approximately 5-10 µm distance above the sample which is scanned in xy-direction during the measurement.

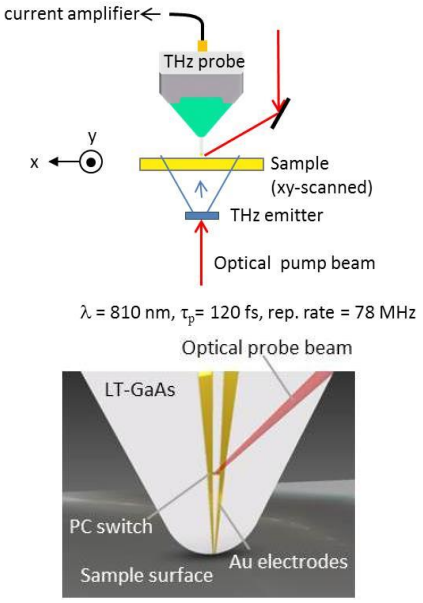

Figure 1: Schematic of the central measurement configuration including the optically excited THz emitter and near-field microprobe which is additionally shown in the enlargement below.

The samples used in this work for the laser-doping structures were processed as follows: First, an acid etch of the *p*-type mc-Si wafer is used to remove saw damage and to texture the surface in order to reduce incident light reflection. Then thermal diffusion of phosphorus doping in a furnace with $POCl_3$ gas creates a lightly doped n^+ emitter region. The remaining phosphorous silicate glass (PSG) layer on the wafer serves as a dopant source for

laser doping. Next, the wafers were processed using a pulsed neodymium aluminum garnet laser (Nd:YAG) having a wavelength λ = 532 nm and pulse repetition frequency 15 - 200 kHz. The laser irradiation locally drives the lattice temperature above the melting point and the diffusion takes place in the liquid phase. The diffusion is up to 10 orders of magnitude faster than in the solid state, thus enabling deep junctions. Subsequent to the laser pulse, the molten silicon cools, re-crystallizes epitaxially, and forms a thin, highly phosphorus doped n^{++} emitter. After the emitter diffusion, the PSG on the surface was removed and a a-SiN$_x$:H anti-reflection coating (ARC) layer is deposited.

The IBC cells of this investigation were processed according to the shown flowchart in Fig. 2: n-type Czochralski (Cz) Si-wafers were textured resulting in random pyramids, and tube diffusions were used to create the rear-side emitter, back-surface field (BSF) and the front-surface field (FSF), as indicated in the scheme below. Further details can be found in an earlier publication [3]. A similar approach was used for the patterns in the test structures investigated. It should be mentioned that the front and rear side of these structures are textured and passivated.

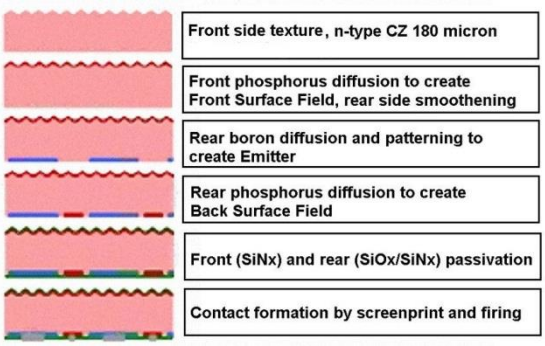

Figure 2: Process flow of screen-printed IBC cells.

3 RESULTS AND DISCUSSION

3.1 Laser-doping

In a first step the 4pp measured sheet resistance of a laser-doped mc-Si sample is compared with data from the THz microprobe system. THz transmission amplitude data $T(\omega)$ are converted into sheet conductivity values σ_{sh} following the Tinkham formula [4]:

$$T(\omega) = \frac{E_{substrate+layer}(\omega)}{E_{substrate}(\omega)} = \frac{1}{1 + \sigma_{sh}\frac{Z_0}{n(\omega)+1}} \quad , \qquad (1)$$

where $E_{substrate}$ and $E_{substrate+layer}$ are the transmitted THz field amplitudes of the substrate without and with doping layer, respectively. $Z_0 \approx 377\ \Omega$ is the impedance of free-space. n = 3.39 is the refractive index of the silicon substrate we consider under negligence of spectral dispersion. Since a comparison measurement without doping layer is not available in this case, a reference value $\sigma_{sh} = \sigma_{sh,ref}$ determined by a 4pp-measurement in the outer unprocessed emitter. This sheet conductance, $\sigma_{sh,ref,}$ together with its corresponding transmitted THz field amplitude can be used to relate the transmitted THz field amplitude on position i(x,y) anywhere on the sample to its corresponding sheet conductance, $\sigma_{sh,i}$, using equation 2.

$$\sigma_{sh,i} = \frac{n+1}{Z_o}\left[\frac{E^{ref}{}_{substrate+layer}}{E^{i}{}_{substrate+layer}}\left(1 + \sigma_{sh,ref}\frac{Z_o}{n+1}\right) - 1\right] \qquad (2)$$

The calibration principle is also graphically explained in Fig. 3. It is worth mentioning that in case background doped substrates are used, no 4-pp reference measurements are required to determine the sheet conductance.

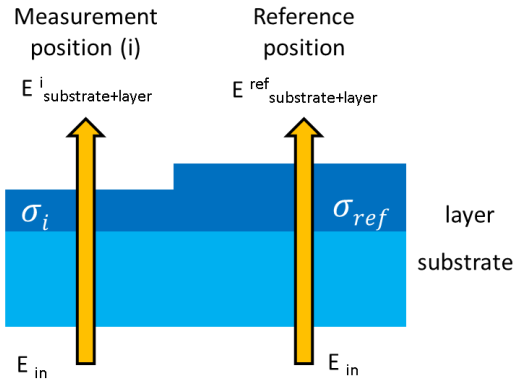

Figure 3: Schematic illustration of the applied calibration principle. E_{in} is the field amplitude of the incoming THz radiation, $E^{i}_{substrate+layer}$ is the field amplitude of the transmitted THz radiation at measurement position i (x,y).

It has been shown by Herrmann et al. [5] that the relative transmission coefficient of a comparable surface-doping layer on a silicon wafer is nearly frequency independent in the range of 0.1-1 THz which is transmitted in our set-up. For sheet resistance determination we can hence in most cases neglect the frequency dependency and consider only the modification of the peak amplitude transmission of the THz pulse.

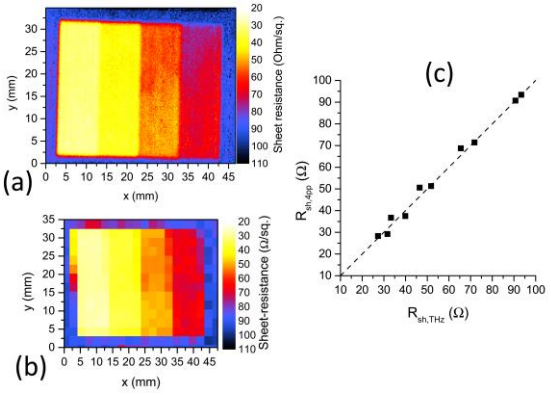

Figure 4: Comparison of sheet resistance measurements of laser-doped mc-Si samples with a variation of pulse energy density by (a) THz microprobe system and (b) 4pp. (c) Correlation between THz- and 4pp-generated R_{sh}-mean-values obtained from two measurement rows.

The laser-doped sample used for this study contains four fields with different sheet resistances generated through variation of laser pulse energy density. In Fig. 4 (b) the sheet resistance map measured by 4pp is shown. It contains 300 pixels probed at 5s/pixel in 25 min. The sheet resistance of the base emitter is approx. 95 Ω/sq. The R_{sh}-map obtained with the THz microprobe system is shown in Fig. 4 (a). Here, it took only 2.5 min to measure the image: 26.3 kpixel at a speed of 5ms/pixel – a three orders of magnitude speed advantage over the 4pp

technique. The maximum deviation between the 4pp and THz based R_{sh}-values is 10 % as shown by the correlation graph in Fig. 3 (c).

To further show the potential of the THz microprobe system and the need of higher resolutions an exemplary measurement of a laser-doped mc-Si sample without an overlap of pulses is shown in Fig. 5. For this study a double-gaussian shaped beam profile has been used [6].

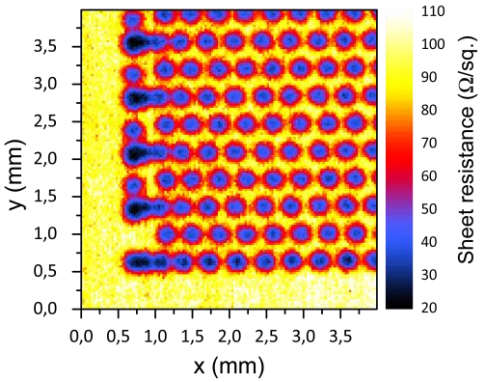

Figure 5: Exemplary sheet resistance image (30 µm scan steps) measured on a laser-doped mc-Si sample.

We can clearly see that the middle part of the laser spots has a lower resistivity due to higher intensities in the centre of the double-gaussian beam profile leading to higher temperatures and a deeper melt. Very striking are the darker spots on the left. These spots, with minimum sheet resistance in the order of 20 Ω/sq, are attributed to a double exposure by laser pulses. These effects cannot be visualized by the 4pp system due to insufficient resolution.

3.2 IBC cells and pn-junction test structures

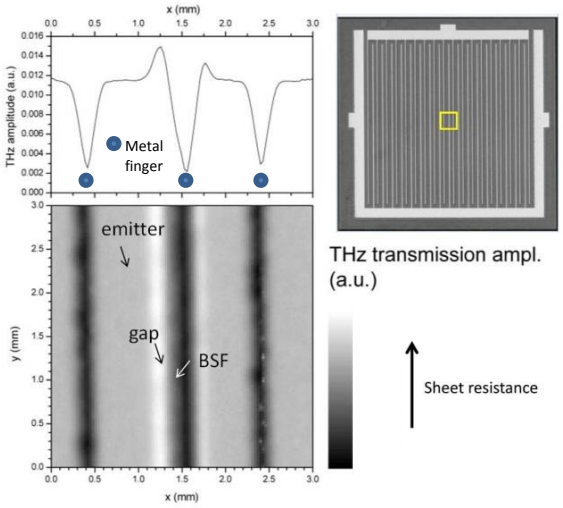

Figure 6: (left bottom) THz transmission measurement of a 3x3 mm large area of the IBC cell sample and corresponding line plot (upper left) for y = 1.5 mm. (upper right) Camera image of the investigated cell and measured area as marked by the yellow square.

For IBC cells, the typical size of the diffused features is in the same range as for a selective emitter, or even smaller. The typical areas of interest comprise a *p+* doped emitter, an *n+* doped BSF and if applicable an *n*-type gap, which can be used as the reference area. For the gap, it has to be kept in mind that the sheet conductance is the sum of the wafer and FSF conductance.

In Fig. 6, the THz transmission imaging of a part of an IBC cell sample is shown. The black lines indicate the screen-printed metallization, which blocks the THz transmission. The gap appears in white, since the doping is relatively low leading to high THz transmission. The BSF, although not well visible due to the presence of the metal fingers, appears to be darker than the emitter. This is in agreement with 4pp sheet resistance measurements of the emitter and BSF on large reference areas, which revealed a BSF conductance which was significantly higher than the emitter conductance. The THz intensities of the two gap areas are different. This can be caused by the difference in gap width together the limited resolution of the THz measurement in this specific set-up where the metallization does not allow close proximity of the probe-tip. It has been observed that the vicinity to metal lines can make thermography measurements largely blind to the carrier density distribution at comparable structures [7]. However, using THz microprobing this information is still accessible, even though the resolution is slightly reduced because of a limited probe-tip approximation.

In the next step, three different types of test structures have been systematically investigated to analyze lateral *pn*-junctions. Double side textured test structures with i) homogeneously diffused patterns, ii) with selectively diffused lines without a gap and (iii) selectively diffused lines with a gap. The schematic structure of the homogeneously diffused sample is shown in Fig. 7. At the top, a schematic cross-section of the processed sample is shown and the corresponding THz imaging of the sample is demonstrated at the bottom. For the first time, it is possible to measure the sheet-resistance distribution and local inhomogeneity of the fingers on these textured surfaces in a practical way. The average values are close to the values measured on large-area samples.

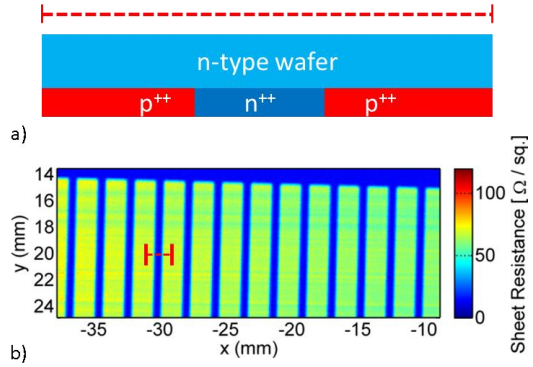

Figure 7: (a) Schematic structure cross-section of the processed sample of homogeneously diffused p- and n-type surfaces without gap. (b) THz imaging results showing the sheet resistance of the lines.

In addition, we can also determine inhomogeneities in the emitter areas (p^{++}). These inhomogeneities appear as lines with lower sheet resistances. To confirm that these lines are not measurement artifacts the sample is rotated and the measurement is repeated. In Fig. 8 the THz imaging result of a part of the rotated sample is demonstrated.

Since the direction of the inhomogeneity lines stays the same after sample rotation we can conclude that these features are sample inherent and not a measurement artifact.

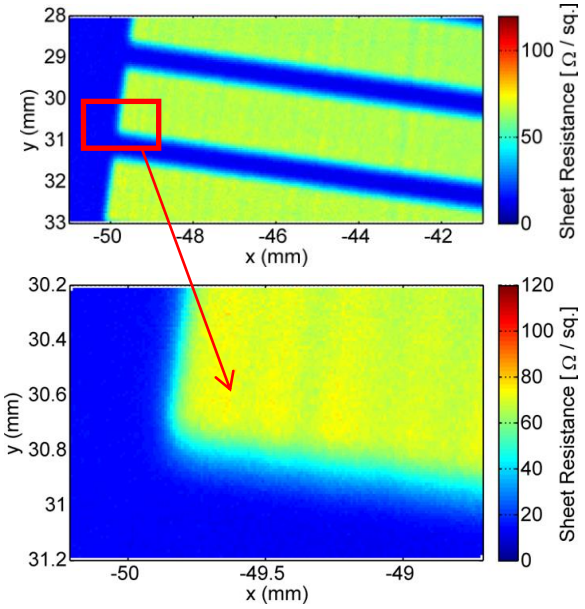

Figure 8: THz imaging of the rotated sample with homogeneous diffusion (n^{++} area is indicated by blue contrast).

We assume that the origin of this inhomogeneity is caused by saw damages of the silicon surface which is generating a slight phase shift of the transmitted THz pulse. This has to be analyzed in detail through further measurements.

In the next step test structures with selectively diffused areas have been investigated as illustrated in Fig. 9. Selective diffusion means in this case that we have highly doped n^{++} and p^{++} lines and around the lines lowly doped regions are obtained as clarified in the schematic of the cross-section in Fig 9b.

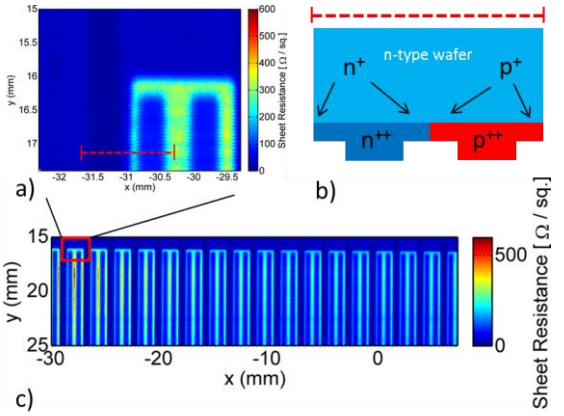

Figure 9: (a) Detail THz Rsh image with dashed line of the test structure. **(b)** Schematic structure cross-section of the selective diffused sample illustrating cross-section along dashed line in **(a)**. **(c)** Overview THz R_{sh} images.

The THz imaging of the sample shows on the one hand the sheet-resistance of the heavily and lowly doped lines and on the other hand some further prominent features. On this sample we observe as well a material inhomogeneity in form of stripes almost orthogonal to the doped lines/fingers/features similar to the homogeneously diffused sample without selective doping structures. On the left side of the THz imaging some reddish regions with high sheet resistances >400 Ω/sq. can be observed. This reveals that the pattering process used for the test structure is not homogeneous.

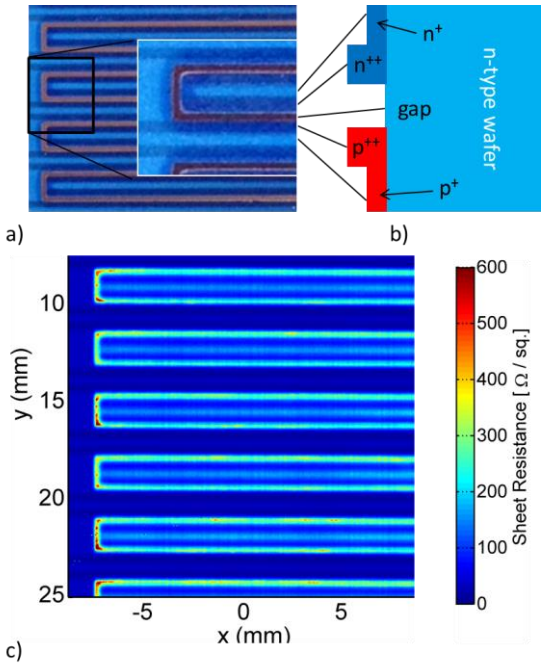

Figure 10: (a and b) Schematic structure of the selective diffused sample with a gap and its photograph. (c) THz R_{sh} image.

As a last example, we investigated a selectively diffused sample with a gap between the *p*- and *n*-type doped regions. In Fig. 10 the schematic structure of such a sample together with a photograph is shown. The difference between this sample and the selectively diffused sample is that the p^{++} and n^{++} regions are separated by a gap produced by selective etching of a line, generating a local sheet resistance increase. The THz imaging technique enables the visualization and R_{sh}-measurement of such a structure. Similar to the other experiments it represents the sheet resistance of different parts of the sample and shows that the selective etching of the lines, which are in this case the gap, leads to high sheet resistances resulting in an electrical separation of the two doped regions. However, also in this case the etching is inhomogeneous and causes regions with different sheet resistance in the gap region. Like in the previous sample, a detailed look at the THz images reveals a periodic structure in vertical direction to the doped lines.

3 CONCLUSION

The THz measurements confirm the observations of the 4pp sheet resistance mapping and microscopic analysis. The reliability of the quantitative values is already very promising. The resolution and measurement speed of the THz microprobe system surpasses conventional 4pp-mapping by several orders of magnitude.

From the IBC process perspective we can conclude that THz imaging shows small-scale doping inhomogeneities in the (selectively) diffused areas and gap regions typical for IBC cell processing, which allows for direct feedback for process tuning. The THz measurements are suitable for doped and textured surfaces, practical to perform in terms of sample preparation and measurement time while it features a measurement resolution that is unusually high compared to other mapping methods like the traditional four-point-probe method. This makes the method a valuable asset for solar cell research and development.

REFERENCES

[1] A. Safiei, R. Derix, S. Suckow, H. Koch, U. Breuer, T. M. Pletzer, K. Wolter and H. Kurz, "Generation of Defect-Related Acceptor States by Laser Doping," Solar Energy Materials and Solar Cells **106**, 2-6, (2012).

[2] M. Wächter, M. Nagel and H. Kurz, "Tapered photoconductive terahertz field probe tip with subwavelength spatial resolution", Appl. Phys. Lett., **95**, 041112 (2009).

[3] M.W.P.E. Lamers et al., "Towards 21% efficient n-Cz IBC based on screen printing", Proc. 26th EUPVSEC (2011).

[4] M. Tinkham, "Energy Gap Interpretation of Experiments on Infrared Transmission through Superconducting Films", Phys Rev. **104**, 845 (1956).

[5] M. Herrmann, M. Tani, K. Sakai, and R. Fukasawa, "Terahertz imaging of silicon wafers," J. Appl. Phys. **91**, 3, 1247 (2002).

[6] A. Safiei, K. Wolter, M. Nagel, H. Windgassen, and H. Kurz, "Evaluation and investigation of laser doping by a double-gaussian shaped beam profile," 39th IEEE Photovoltaic Specialists Conference, submitted (2013).

[7] T. M. Pletzer, M. Lenz, H. Windgassen, and J. Knoch, "Characterization of three dimensional structures in silicon solar cells by spatially resolved illuminated lock in thermography", 38th IEEE Photovoltaic Specialist Conference, Austin, (2012).